Available online at www.sciencedirect.com

ScienceDirect

Energy Procedia 92 (2016) 505 – 514

Energy Procedia

6th International Conference on Silicon Photovoltaics, SiliconPV 2016

Increased light harvesting by structured cell interconnection ribbons: an optical ray tracing study using a realistic daylight model

Hendrik Holst[a,*], Henning Schulte-Huxel[a], Matthias Winter[b], Susanne Blankemeyer[a], Robert Witteck[a], Malte R. Vogt[a], Thomas Booz[c], Fabian Distelrath[c], Marc Köntges[a], Karsten Bothe[a], Rolf Brendel[a,b]

[a]*Institute for Solar Energy Research Hamelin (ISFH), Am Ohrberg 1, 31860 Emmerhal, Germany*
[b]*Dep. Solar Energy, Institute for Solid State Physics, Leibniz University Hannover, Appelstraße 2, 30167 Hannover, Germany*
[c]*Schlenk Metallfolien GmbH & Co. KG, 91154 Roth-Barnsdorf, Germany*

Abstract

A key for increasing the module efficiency is improved light harvesting. The structuring of solar cell interconnection ribbons (CIR) is a promising option for improved light harvesting as it can easily be integrated into current module production. We perform ray tracing simulations of complete PV modules in 3D exhibiting geometric features such as profiled CIR and surface textured cells. We evaluate the increase in module performance by a light harvesting string (LHS) under realistic irradiation conditions with respect to angular and spectral distribution. Using the realistic irradiation for a location in Germany, a location at the polar circle and a location at the equator we simulate the enhancement of short-circuit current density J_{sc} resulting from the use of LHS. Our results show J_{sc} gains between 1.00% and 1.86% depending on the location and module orientation. We demonstrate the applicability of our model by comparing measurements and simulations for a one-cell module that we measure and simulate under various angles of the light incidence.

Peer review by the scientific conference committee of SiliconPV 2016 under responsibility of PSE AG.

Keywords: ray tracing; light harvesting string (LHS); realistic irradiation

* Corresponding author. Tel.: +49-5151-999-644; fax: +49-5151-999-400.
E-mail address: holst@isfh.de

Peer review by the scientific conference committee of SiliconPV 2016 under responsibility of PSE AG.
doi:10.1016/j.egypro.2016.07.134

1. Introduction

In order to increase module efficiency the light harvesting capabilities of the module have to be improved. One option is the use of structured cell interconnect ribbon (CIR) which easily can be integrated within the module production. To optimize the structure of the CIR it is essential to know its impact on the module performance. For this reason one typically measures the current voltage characteristic of the module under standard test conditions (STC). Standard test conditions assume a spectral distribution as defined in IEC 60904-3, Ed. 2.0 with an angular distribution constraint to normal incidence. It has been shown [1,2] that structured CIR have a significant impact on the module performance under these conditions by increasing the generated current density by about 2.5%. The commercial structured CIR from *Schlenk Metallfolien GmbH & Co. KG* evaluated in this paper is named light harvesting string (LHS).

Aiming at reducing experimental efforts and costs for the manufacturing of modules as well as studying the impact of different irradiation conditions we perform optical ray tracing simulations utilizing our in-house ray tracer DAIDALOS [8]. For the modeling of the LHS we utilize a 3D profile extracted from a cross sectional micrograph as well as an associated refractive index of the CIR material. In contrast to literature, where the CIR's optical properties are only modeled by light recovery factors [3] or shading area ratios [4], respectively, this approach enables us to simulate the optical properties for different angles of incidences as well as spectrally resolved.

Moreover, STC differs significantly from the irradiation conditions for realistic photovoltaic (PV) system installations in the field, where the sun moves over the celestial hemisphere, therefore changing its angle of incidence as well as the traversed air mass (i.e. the incident spectral distribution). Thus it is questionable if the performance increase measured under STC is the same for realistic field conditions [5, 6].

Within this work we therefore investigate the light harvesting capabilities of the LHS using optical simulations under realistic irradiation conditions. Using a recently published approach [6, 7] we model the mean annual daylight, including the spectral and angular distribution, based upon measured irradiances for the region of Hamelin, Germany. Also, we create two "artificial" clear-sky representations of the mean annual daylight as found in the region of the polar circle and the equator. Utilizing these models for mean annual daylight we compare the short circuit current density J_{sc} generated by the use of standard CIR and LHS and evaluate the realistic current gain of LHS for these locations.

2. Daylight models

In order to allow for a realistic representation of daylight within a simulation, its spectral and angular distribution has to be modelled. We utilize an in-house developed mean annual daylight model [6, 7] which is based on irradiances that we measured over 14 years (1992 – 2006) in Hamelin, Germany. The measurements were performed using a pair of photopyranometers to obtain the values of horizontal global and diffuse irradiance with a temporal resolution of 5 minutes. Our model includes the impact of the sun's position and clouds on the angular and spectral distribution. However, scattering of light is treated wavelength independent. This means that the spectral impact of e.g. aerosols or seasonal changes in the atmosphere composition are neglected. The result of our approach is a mean annual daylight distribution that models the celestial hemisphere by a partition into solid-angle intervals of 5° azimuth and 5° altitude. Each of these intervals contains its own spectral distribution of diffuse and direct light. Figure 1(a) shows the apparent origin of the light on the celestial hemisphere for the location of Hamelin, Germany. Here, the intervals are colored corresponding to the radiation power density that incidents from the particular solid angle.

Additional to the daylight model for Hamelin, we also generate models for a location at the equator and a location at the polar circle. Contrary to the model for Hamelin, which is based on measured irradiances, these two are based on artificial irradiance data we calculate for both locations using SMARTS [11]. Consequently, for these sources an unclouded sky is assumed. This decreases the fraction of diffuse light in the models considerably. The associated distributions of light incidence angles are shown in Figure 1(b) and 1(c).

Note that due to the neglected clouds, the calculated radiation power density is higher than expected. However, in the simulations all power densities are scaled to a value of 1000 W/m^2 in order to be comparable to AM1.5G, therefore our results only depend upon the spectral and angular distributions of the particular daylight model.

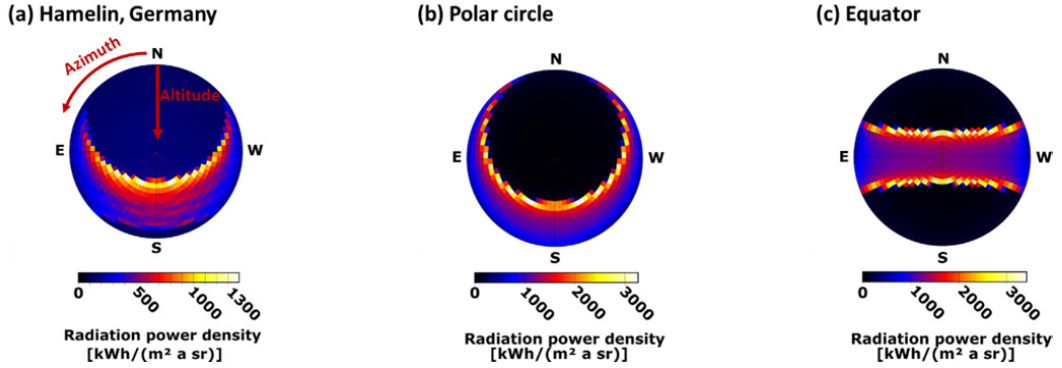

Fig. 1. Partition of the celestial hemisphere into intervals of 5° azimuthal angle (measured from north over east) and 5° altitude angle (measured from horizon to zenith). Each interval is colored corresponding to the mean annual radiation power density expected for the locations of Hamelin, Germany (a), the polar circle (b) and the equator (c).

3. Simulated structures

The task of performing optical simulations on full solar modules is quite complex for two reasons. On the one hand, light can travel lateral distances of several centimeters due to multiple reflections within the module. Different

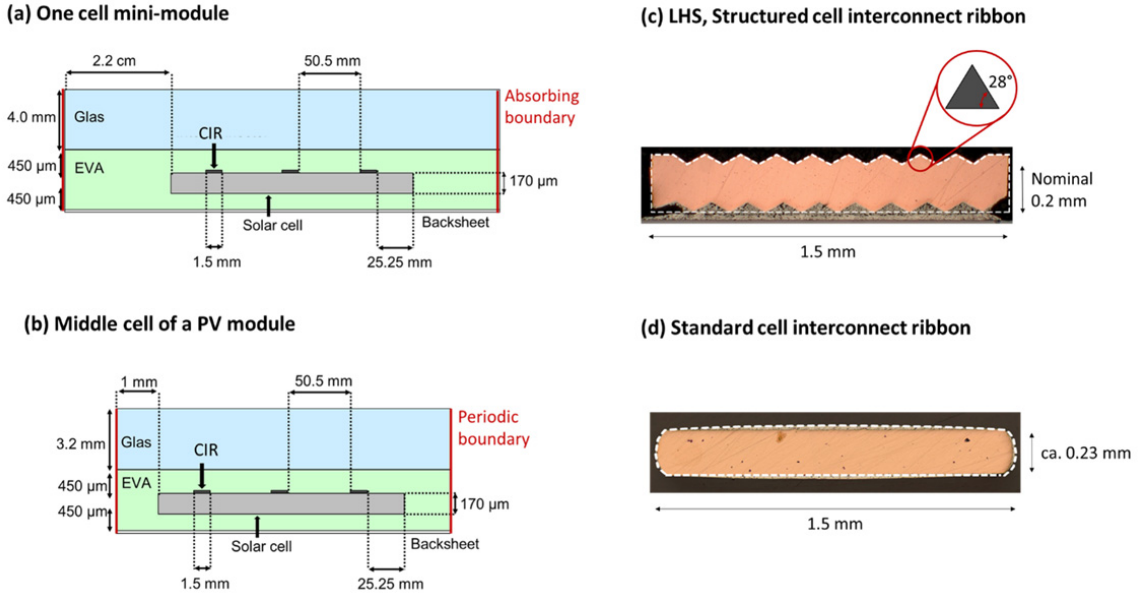

Fig. 2. To represent the geometry (a) of the measured one-cell module a 2.2 cm wide cell-to-edge gap and absorbing boundary conditions are used. For the simulation under realistic irradiation conditions a cell within the middle of a PV module is modelled (b) with a 1 mm wide gap and periodic boundaries. Microscope images of the profiles of the standard CIR (c) and LHS (d) are used to model the shape of the cell interconnect ribbons. Both have similar dimensions with a height of about 0.2 mm and a width of 1.5 mm. The profile shapes used in the simulation are shown by the white dashed outline. Within the simulation, the standard CIR is simulated using the material parameters of the solder alloy, while the LHS consists of silver.

parts of the module are, therefore, optically coupled. This impedes optical simulations based on small unit-cells. On the other hand, the sizes of module components are ranging from the micrometer scale (e.g. the pyramid texture) to the meter scale (e.g. metal frame). Therefore, using large simulation domains leads to a high amount of geometric objects (e.g. each cell's surface is textured with roughly $5 \cdot 10^8$ pyramids). Using our in-house developed ray tracer DAIDALOS [8,9], we are able to utilize a multi-domain algorithm [10] for simulating the whole module geometry.

We simulate two module geometries. For the comparison with current measurements of a one-cell module, the module geometry in Figure 2(a) is used. It includes a cell-to-edge gap of 2.2 cm and absorbing boundary conditions to model the black edges of the produced mini-module. Contrary to that, we use the geometry shown in Figure 2(b) for our simulations of full modules under realistic modelled irradiation conditions. This geometry represents a solar cell within the middle of a PV module, therefore, a 2 mm gap to adjacent cells as well as periodic boundary conditions are used. Note, although not shown in Figure 2(a/b), our geometries include the metal fingers and the random pyramid texture on the cell's top as well as the cell's full-area aluminum rear metallization. The refractive index data and dimension for all module components are listed in Table 1.

3.1. Geometric model of the cell interconnection ribbon

We simulate a standard CIR as well as a structured LHS. The LHS is modelled according to profile measurements of the manufacturer that are shown in Figure 2(c). The profile of the standard CIR was measured in-house and modelled as shown in Figure 2(d). The material parameters (i.e. the complex index of refraction) of the solder alloy (Sn62.5/Pb36/Ag1.5) were determined by spectroscopic ellipsometry and are given in appendix A.

Table 1. Module components, optical properties and thicknesses as used in experimental test modules and ray tracing simulations.

Module component	Material	Thickness
Glass	Low iron float glass [13]	4.0 mm
Encapsulant	EVA (Data from [14] smoothed and adjusted to [15] for wavelength over 350 nm)	450 µm above and below the cells
Std. CIR	Solder alloy, n and k determined by in-house measurements (Appendix A)	230 µm (1.5 mm wide)
LHS	Ag [16]	200 µm (1.5 mm wide)
Finger	Ag [16]	20 µm
Cell front ARC	SiN [17]	75 nm
Cell	Si (n [17]; k [18])	170 µm
Cell rear side dielectric	SiN [17]	200 nm
Cell full area rear metallization	Al [19]	20 µm
Backsheet	White backsheet [17]	300 µm

4. Simulations

4.1. Comparison with incident angle dependent measurements on a one-cell module

We measure the current of a one-cell module, contacted either with LHS or standard CIR, under varying incident angles of the light (-80° to +80°) and compare these results with our simulations. The one-cell module is shown in Figure 3(a) with its side edges colored in black to prevent light from passing this boundary. The corresponding module geometry used in our simulation is shown in Figure 2(a).

The angle dependent current measurements are performed using a class AAA flasher (HALM GmbH). While the light source is fixed, the one-cell module is tilted around a rotation axis and the generated module current density J_{sc} is measured. This is done in two configurations, in the first one the module is tilted around an axis parallel to the CIR, leading to an angle variation across the CIRs (Figure 3(b)). In the second one, the tilt is done around an axis perpendicular to the CIR, introducing an angle variation along the CIRs (Figure 3(c)). These angle variations are

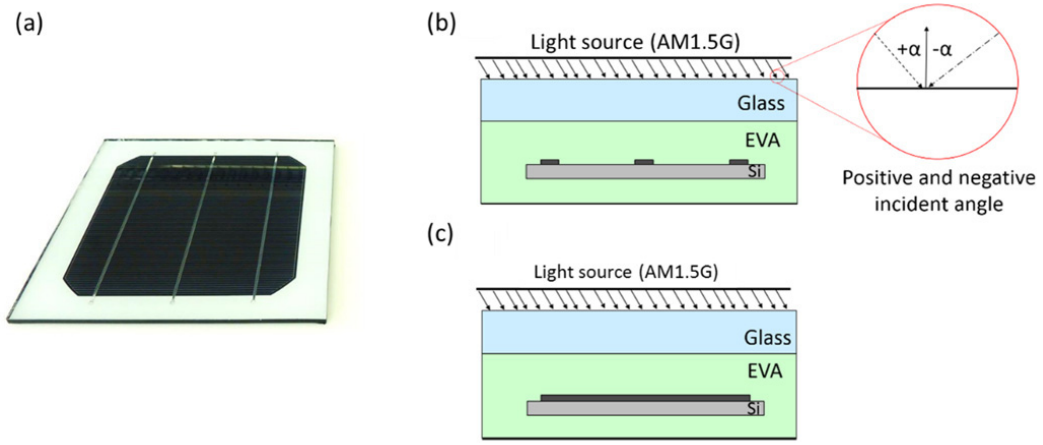

Fig. 3. A one-cell module (a) is built to measure the generated short circuit current density J_{sc} under varying incident angles. These are varied by tilting the module either around a rotational axis parallel to the middle cell interconnection ribbon, resulting in an angle variation across the CIRs (b) or by an axis perpendicular to the CIRs, resulting in an angle variation along them (c).

then modelled within the optical simulation to determine the generated short circuit current density when using standard CIR ($J_{sc,std.}$) and LHS ($J_{sc,LHS}$). The relative J_{sc}-gain reached of LHS is calculated as the ratio $J_{sc,LHS}/J_{sc,std}$.

In Figure 4, the simulated gain in the short-circuit current density J_{sc} is compared to the one calculated from the measurement. The simulated results are in good agreement with the measurement. However, the small changes in current resulting from the use of LHS compared to standard CIR, in the range of 0.1 mA/cm^2, result in a significant measurement uncertainty of the J_{sc}-gain. Especially for large incidence angles the measurement uncertainty is drastically increased. The reason for this is twofold, the solid angle under which the module is seen from the light source is reduced resulting in a reduced intensity of the incident light and a large fraction of the incident light is reflected at the air/glass-interface.

Considering the J_{sc}-gain of a module tilted around an axis parallel to the CIR (Figure 4(a)), the curve can be best described by a separation into three parts. For an incident angle from 0°-20°, light that incidents on the LHS is reflected under an angle that leads to total reflection at the glass/air interface and is reflected back towards the cell. The three cell interconnect ribbons cover an area of about $(3 \times 1.5 \cdot 156)$ mm^2 and occupy a fraction of about 2.9% of the cell's surface. As shown in the appendix (Table 2), the average reflectivity of the embedded LHS under normal irradiance is about 89.7% within the simulated wavelength range. Therefore under optimum conditions, i.e. all light reflected at the air/glass interface is absorbed by the cells, this would lead to about 2.6% J_{sc} gain under normal incidence. As can be seen from Figure 4, the J_{sc}-gain is about 1.8 % due to three effects. First, some of the reflected light is absorbed within the EVA and the SiN_x coating on the cell's surface after reflection. Second, not all light that reaches the cell is actually absorbed but may be reflected instead. And third, reflection at the standard CIR is not fully specular but scatters a part of the light which also gets reflected back onto the cell.

If the module is tilted around an axis parallel to the CIRs (Figure 4, left) there is a sudden decrease in the achieved J_{sc}-gain for incident angles larger than 20°. This occurs because light reflected by the LHS is no longer totally reflected by the glass/air interface and therefore can leave the module. Finally, for incident angles larger than about 45° degree, the reflection decreases further because light which hits the LHS under an incident angle (measured against the module normal) larger than the LHS structure angle of 28° is redirected by the LHS structure

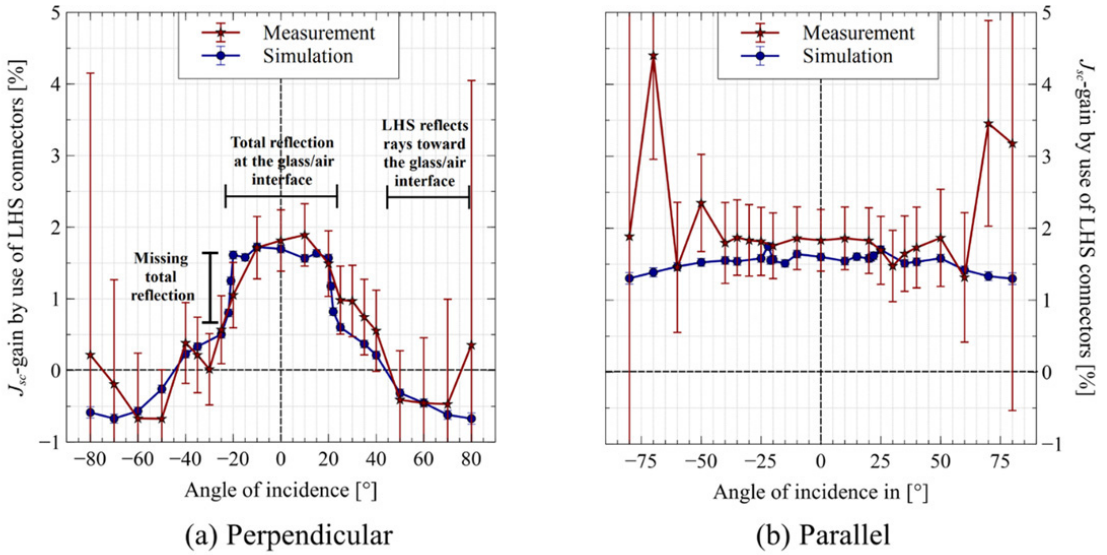

Fig. 4. A module tilt around the parallel axis (left) shows a significant decrease in J_{sc}-gain for light with incident angles bigger than 20° on the module's surface. This is due to the fact that a reflection of these rays at the LHS does not lead to total reflection at the glass/air-interface. In the case, of a module tilt around the perpendicular (right) this effect does not occur, resulting in a nearly constant J_{sc}-gain.

toward the glass/air interface, easing the transmission out of the module. Due to this effect the J_{sc}-gain falls below zero, i.e. the generated short current density is smaller for a module with LHS than for one with standard CIR, at such large incident angles.

In the case of a tilt variation around an axis perpendicular to the CIRs (Figure 4(b)), a nearly constant J_{sc}-gain of about 1.8% is observed. In this case the projected angle within the plane perpendicular to the LHS does not change. The light harvesting structure can therefore function as intended, i.e. inducing total reflection at the glass/air interface, for all angles of incidence.

4.2. Comparison of J_{sc} gain at different locations on the earth surface

The results presented in the previous section show a J_{sc}-gain of about 1.8% for a usage of LHS under normal incidence. Note, that the measured one-cell module (Figure 2(a)) has a wide gap of 2.2 cm as well as absorbing boundary conditions, which is possibly the reason for the deviations between the measured value and the literature value of about 2.5% under STC [1, 2].

However, as is also shown in Figure 4(a), J_{sc}-gain quickly decreases for incidence angles larger than 20° dependent on the module orientation. To simulate the impact of LHS under realistic conditions, where light is incident from several directions, we make use of the above presented daylight model. We simulate the short-circuit current density J_{sc} of a middle cell within a solar module which is either contacted with standard CIR or LHS. For these simulations we use the module geometry shown in Figure 2(b). To simplify the simulation we neglect contributions from the modules edge area (e.g. reflection at the metal frame) by applying periodic boundary conditions on the domain boundaries of the simulated module geometry. Additionally, to be comparable to AM1.5G spectrum with respect to the total radiation power density the power densities of the daylight sources are scaled to 1000 W/m^2.

Within our simulations we consider the two module orientations shown in Figure 5(a/b). In the south-north (SN) orientation of the CIR, the sun's path over the module crosses the CIR, while it goes along them in the east-west (EW) orientation. Furthermore, each module has an optimal tilt angle towards south, with 35° for the region of Hamelin, 48° for the polar circle and 0° for the equator. The values of the J_{sc}-gain resulting from these simulations are shown for all three locations as well as for both orientations in Figure 5(c).

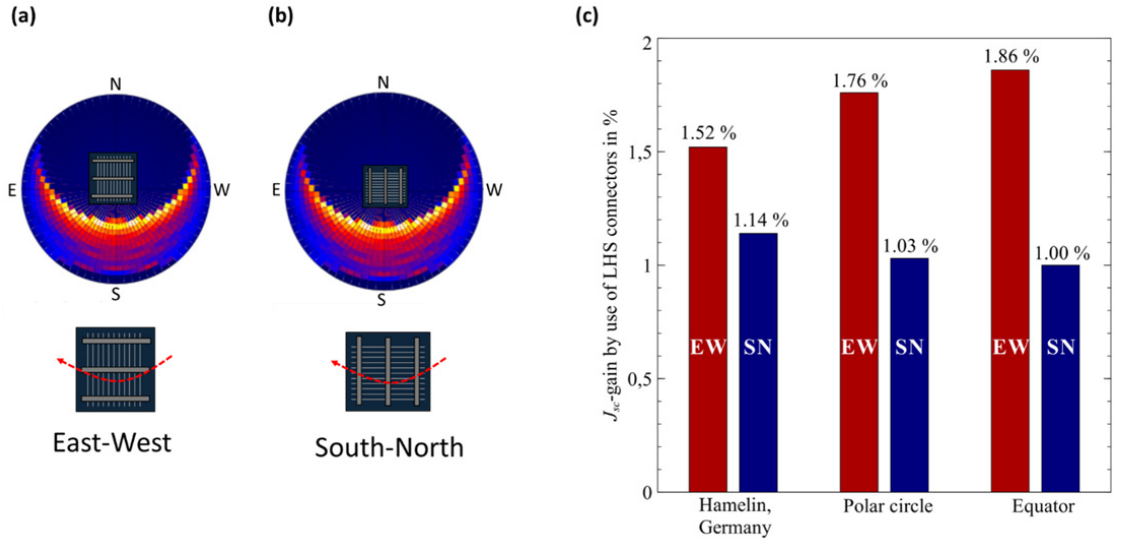

Fig. 5. The simulation is performed with two module orientations. In the east-west orientation (a) the sun's path goes along the CIRs, while in the south-north orientation (b) it crosses them. The associated gain in J_{sc} by using LHS at the different locations (c) is highest for an EW orientation. It correlates with the ratio of diffuse to direct light, which is lowest for the light sources at the equator (diff./dir.=0.15) and at the polar circle (diff./dir.=0.2).

Figure 5c shows that a higher J_{sc}-gain can be reached in EW orientation than in SN orientation for any of the simulated locations. The reason for this is that the sun's path going parallel along the CIR for an EW orientated module, according to Figure 4b, results in a nearly constant J_{sc}-gain. Contrary to that, a SN orientation results in a significant decreased J_{sc}-gain in the morning and evening hours.

The maximum reachable J_{sc}-gain depends on location. It is about 1.86%, for the equatorial region and 1.76% at the polar circle. For Hamelin it's only 1.52%. For this latter case, measured irradiance data was used to create the irradiation model, which therefore includes light scattering by clouds. As a consequence the ratio of diffuse to direct irradiance is 0.47. The diffuse fraction is significantly smaller for the artificial sources which neglect the impact of clouds, resulting in a ratio of 0.2 for the polar circle and 0.15 for the equatorial region. Some of this diffuse light incidents from small altitude angles, e.g. from near the horizon. In EW orientated modules, this light hits the LHS under an angle that does not allow for a succeeding total reflection at the glass interface (as shown in Figure 4(a)), consequently resulting in a decrease in J_{sc}-gain.

In Figure 5(c) it can be observed that this impact of light from small altitudes is reversed for SN orientated modules. The gain in J_{sc} increases for SN orientated modules from the region of the equator (1%) over the polar circle (1.03%) to the region of Hamelin (1.14%). A possible explanation for this is that SN orientated modules allow for an LHS induced total reflection at the glass/air interface only for a small interval of incident angles between 0° to 20° (Figure 4(a)). Thus, it is preferable for these modules when direct light that initially incidents under larger angles of incidence is scattered over the celestial hemisphere with a fraction also scattered into the acceptable angle interval. Consequently, the J_{sc}-gain increases with the fraction of diffuse irradiance.

4.3. Monthly resolved J_{sc} gain for the region of Hamelin

To investigate the impact of light impinging from small altitude angles on the performance of EN and SN orientated modules, respectively, we simulate the monthly resolved J_{sc}-gain for the region of Hamelin. While the module geometry remains unchanged with respect to the previous section, the mean annual daylight for Hamelin is

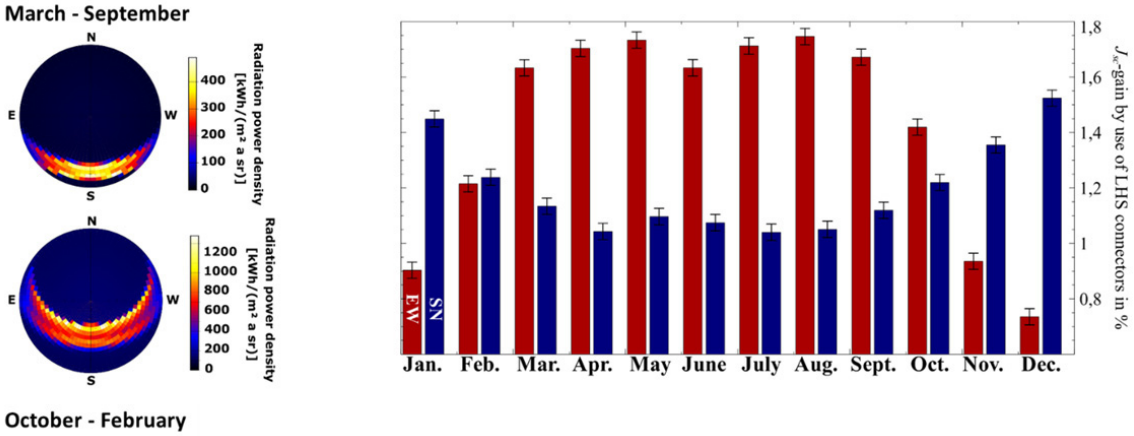

Fig. 6. The angular distribution of incident light in the region of Hamelin varies significantly between the summer (March to September) and the winter (October to February). This angular variation has a significant impact on the performance of the LHS during the twelve month of a year. While EW orientated modules profit from direct light in the summer with increased J_{sc}-gain compared to SN orientated ones, this is inverted in the summer where the incident light is coming from small altitude angles.

split into twelve mean monthly models. Utilizing this models, we repeated the simulation of the expected J_{sc} – gain for each of the twelve months. The result of these simulations is shown in Figure 6(right), which presents the values of J_{sc}-gain achieved when using LHS instead of standard CIRs during the particular month. As can be seen, an EN orientation of the module results in a J_{sc}-gain higher than about 1.6% in the months from March to September. Here it clearly outweighs the SN orientated modules with a J_{sc}-gain of slightly above 1%. This is changed from November to January in which the EN orientated modules suffer from the flat incident angles resulting in a J_{sc}-gain lower than 1%, while the SN orientated modules still provide a J_{sc}-gain higher than 1.2%. This is, again, due to a higher ratio of diffuse light in winter than in summer.

5. Summary and conclusion

We investigated the impact of the LHS under realistic irradiation by both, experiment and simulation. Measurements were performed on solar mini-modules. For the optical simulations we presented a geometric model of a mini-module and a full-scale module. The modules included either cells with standard CIR and LHS. The shape of the CIR in the geometric models were based on measured profiles. Calculations using these models agree well to incident angle dependent measurements. Simulations and measurements show that a gain in J_{sc} of almost 2%, compared to the use of standard CIR can be reached by the usage of LHS under optimal conditions. These values are significantly affected by the angle of incident and the orientation of the PV modules, whereby LHS benefit from an orientation where the incident light moves along the CIR. Using a realistic model of daylight at three locations we investigated the impact of varying irradiation conditions on the light harvesting capabilities of the LHS. In correspondence with the angle dependent measurements, these simulations show a J_{sc} gain of 1.86% for a location on the equator under optimum module orientation. The results show, that the angle under which light hits the LHS has a significant impact on its performance. Here, experiments and simulation are performed with a glass having a flat air/glass-interface. Structured glass will change the angle of the light ray by refraction. Therefore, in case of structured glass surface the gain in current might change.

To conclude, our simulations show that the LHS provide a significant 1.8% gain in short-circuit current J_{sc} under STC as well as realistic irradiation conditions compared to standard CIR. However, this gain is influenced by the orientation of the modules as well as the prevailing ratio between diffuse and direct light at the particular location. While locations with mostly direct light and an optimal module tilt are expected to profit from a J_{sc}-gain of almost 2%, this will be slightly less 1.5% for regions with about 50% of diffuse irradiation as in central Europe. For all three locations our simulations demonstrated that an orientation of the module where the CIR lie in EW- direction is preferable to a SN-orientation.

Appendix A. Optical data of cell interconnection ribbon

In order to allow for a realistic modeling of the standard CIR, we determined the refractive index of the (Sn62.5/Pb36/Ag1.5) solder alloy on its surface with spectroscopic ellipsometry measurements. The wavelength dependent values are shown in Table 2. Additionally, the reflectivity under normal irradiation, simulated for both CIR types within the EVA, is shown in the table. Here, the wavelength range is constraint to the wavelength interval used within the simulation.

Table 2. Values of the index of refraction (n) and the extinction coefficient (k) measured for the solder alloy (Sn62.5/Pb36/Ag1.5) using ellipsometry measurements as well as the reflectivity for std. CIR and LHS embedded in EVA, simulated for the case of normal irradiation.

	Refractive index of the (Sn62.5/Pb36/Ag1.5) solder alloy		Simulated reflectivity of the CIR when embedded in EVA	
Wavelength[nm]	Index of refraction n	Extinction coefficient k	Std. CIR[%]	LHS[%]
251	0.372	1.799	-	-
301	0.422	2.321	71.45	8.31
350	0.555	2.854	72.06	73.87
400	0.782	3.294	70.88	83.53
450	1.008	3.721	69.74	90.54
501	1.331	4.019	66.74	93.18
550	1.569	4.242	64.84	94.26
600	1.793	4.427	65.12	95.31
651	1.970	4.546	64.12	96.04
700	2.041	4.650	64.39	96.29
750	2.046	4.811	66.57	96.81
800	2.047	5.044	67.85	97.03
849	2.075	5.305	70.39	97.41
900	2.135	5.578	71.87	97.24
950	2.213	5.841	73.22	97.51
1001	2.296	6.086	73.54	97.58
1050	2.376	6.316	73.55	97.15
1099	2.447	6.535	75.18	97.70
1149	2.509	6.749	76.73	97.18
1204	2.565	6.986	76.16	97.34
1253	2.602	7.198	-	-
1301	2.630	7.413	-	-
1350	2.649	7.632	-	-
1404	2.660	7.886	-	-
1451	2.663	8.120	-	-
1499	2.660	8.360	-	-
1551	2.652	8.640	-	-
1598	2.641	8.897	-	-
1649	2.626	9.196	-	-
1695	2.611	9.470	-	-

References

[1] Zemen, Y. et al,“ Performance and yield evaluations of c-Si modules built with reflective interconnectors”, EUPVSEC, 2015
[2] Schneider, J. et al (2014), Combined effect of light harvesting strings, anti-reflective coating, thin glass, and high ultraviolet transmission encapsulant to reduce optical losses in solar modules. Prog. Photovolt: Res. Appl., 22: 830–837. doi:10.1002/pip.2470
[3] Witteck, R. et al.., "Optimized Interconnection of Passivated Emitter and Rear Cells by Experimentally Verified Modeling," in Photovoltaics, IEEE Journal of , vol.PP, no.99, pp.1-8
[4] Shu Zhang et al., "335Watt world record P-type mono-crystalline module with 20.6 % efficiency PERC solar cells," in Photovoltaic Specialist Conference (PVSC), 2015 IEEE 42nd , vol., no., pp.1-6, 14-19 June 2015
[5] Müllejans, H. et al.,”Spectral mismatch in calibration of photovoltaic reference devices by global sunlight method”, Measurement Science and Technology 2005
[6] Winter, M. et al , "Impact of realistic illumination on optical losses in Si solar cell modules compared to standard testing conditions”, EUPVSEC, 2015
[7] Ernst, M. et al, “SunCalculator: A program to calculate the angular and spectral distribution of direct and diffuse solar radiation”, *to be published*
[8] Holst, H., Altermatt, P.P. and Brendel, R., ”Daidalos - A plugin based framework for extendable ray tracing”, Proceedings of the 25th EUPVSEC, 2150 (2010).
[9] Holst, H. et al, “Application of a new ray tracing framework to the analysis of extended regions in Si solar cell modules”, Energy Procedia 38, 86 (2013).
[10] Winter, M. et al , "Combining structures on different length scales in ray tracing: Analysis of optical losses in solar cell modules", NUSOD 2014, pp.167-168, 1-4 Sept. 2014
[11] Gueymard, C., “An anisotropic solar irradiance model for tilted surfaces and its comparison with selected engineering algorithms”, Solar Energy, 1987
[12] Gueymard, C., SMARTS2, A Simple Model of the Atmospheric radiative Transfer of Sunshine: Algorithms and performance assessment Florida Solar Energy Center, 1995
[13] M. R. Vogt et al: “Measurement of the optical constants of soda-lime glasses in dependence of iron content, and modeling of iron-related power losses in crystalline Si solar cell modules”, IEEE Journal of Photovoltaics (2016), vol. 6, no.1: pp.111-118.
[14] McIntosh, K.R et al., "An optical comparison of silicone and EVA encapsulants for conventional silicon PV modules: A ray-tracing study," in Photovoltaic Specialists Conference (PVSC), 2009 34th IEEE , vol., no., pp.000544-000549, 7-12 June 2009
[15] Ohl, S., Hahn, G. “Increased internal quantum efficiency of encapsulated solar cells by using two-component silicone as encapsulant material The compiled state-of-the-art of PV solar technology and deployment”, 23rd European Photovoltaic Solar Energy Conference,2008
[16] Palik, E. D.: Handbook of Optical Constants of Solids. Academic Press Inc.,1985
[17] Vogt MR. Development of Physical Models for the Simulation of Optical Properties of Solar Cell Modules. Phd thesis Leibniz University Hannover 2015.
[18] Schinke, C. et al: “Uncertainty analysis for the coefficient of band-to-band absorption of crystalline silicon”, AIP Advances (2015), vol. 5(6): pp. 067168.
[19] Shiles, E. et al: ‘Self-consistency and sum-rule tests in the Kramers-Kronig analysis of optical data: Applications to aluminum’. Physical Review B (1980), vol. 22(4): pp. 1612–1628.